

Flow past a square cylinder at low Reynolds numbers

Subhankar Sen¹, Sanjay Mittal^{2,*},[†] and Gautam Biswas¹

¹Department of Mechanical Engineering, Indian Institute of Technology Kanpur, Kanpur-208 016, India

²Department of Aerospace Engineering, Indian Institute of Technology Kanpur, Kanpur-208 016, India

SUMMARY

Results are presented for the flow past a stationary square cylinder at zero incidence for Reynolds number, $Re \leq 150$. A stabilized finite-element formulation is employed to discretize the equations of incompressible fluid flow in two-dimensions. For the first time, values of the laminar separation Reynolds number, Re_s , and separation angle, θ_s , at Re_s are predicted. Also, the variation of θ_s with Re is presented. It is found that the steady separation initiates at $Re = 1.15$. Contrary to the popular belief that separation originates at the rear sharp corners, it is found to originate from the base point, i.e. $\theta_s = 180^\circ$ at $Re = Re_s$. For $Re > 5$, θ_s approaches the limit of 135° . The length of the separation bubble increases approximately linearly with increasing Re . The drag coefficient varies as $Re^{-0.66}$. Flow characteristics at $Re \leq 40$ are also presented for elliptical cylinders of aspect ratios 0.2, 0.5, 0.8 and 1 (circle) having the same characteristic dimension as the square and major axis oriented normal to the free-stream. Compared with a circular cylinder, the flow separates at a much lower Re from a square cylinder leading to the formation of a bigger wake (larger bubble length and width). Consequently, at a given Re , the drag on a square cylinder is more than the drag of a circular cylinder. This suggests that a cylinder with square section is more bluff than the one with circular section. Among all the cylinder shapes studied, the square cylinder with sharp corners generates the largest amount of drag. Copyright © 2010 John Wiley & Sons, Ltd.

Received 10 April 2010; Revised 31 July 2010; Accepted 2 August 2010

KEY WORDS: square cylinder; stabilized finite-element; separation Reynolds number; bluffness

1. INTRODUCTION

The analysis of external flow past a square cylinder is a key to various engineering applications. An example of such an application is the design of buildings. Most experimental [1, 2] and numerical studies [2–9] concerning the external flow past a stationary square cylinder have been carried out at moderate to high Reynolds numbers. In this regime, the flow is unsteady. Characteristics of the steady confined flow past a square cylinder at zero incidence (we refer to the cylinder configuration of zero or normal incidence as ‘symmetric’) have recently been reported by Breuer *et al.* [10]. They presented results for $Re = 0.5$ –300 in two-dimensions. The results were computed via finite-volume and lattice-Boltzmann simulations. A blockage of 0.125 was used. The blockage, B , is the ratio of the cross-stream projection of the square (edge length for a symmetric square) to the domain width. Breuer *et al.* [10] conjectured that the steady separation of laminar boundary layer for a square cylinder commences at a Reynolds number smaller than the value for a circular cylinder [11, 12]. Separation was not observed for $Re \leq 1$. Gupta *et al.* [13] employed the finite-difference method and studied the steady flow and heat transfer characteristics in conjunction

*Correspondence to: Sanjay Mittal, Department of Aerospace Engineering, Indian Institute of Technology Kanpur, Kanpur-208 016, India.

[†]E-mail: smittal@iitk.ac.in

with the power-law fluids for $Re = 5-40$ and $B = 0.125$. The flow and heat transfer for power-law fluids in the steady flow regime have also been studied by Paliwal *et al.* [14] for $5 \leq Re \leq 40$. Following a finite-volume formulation, Sharma and Eswaran [15] presented results for $B = 0.05$ and $Re = 1-160$. Heat transfer characteristics of steady flow past a square cylinder have been numerically investigated by Dhiman *et al.* [16] for $1 \leq Re \leq 45$ and $B = 0.05$.

An essential feature of the steady separated flow past a symmetric bluff body is the formation and eventual development with Re of a closed separation bubble attached to its rear surface. In the context of a square cylinder, the bubble length and width are two major parameters indicative of the bubble size. The bubble length, L , is the streamwise distance between the base or rear stagnation and wake stagnation points lying on the wake centerline. The width, w , represents the maximum transverse extent of the bubble bounded by the separation streamlines. Certain features of the steady separated flow past a symmetric square cylinder in the unbounded medium remain unanswered. For instance, no information is available in the literature regarding the value of the laminar separation Reynolds number, Re_s . The separation points for $Re \leq 100$ are known to be fixed at the rear corners of the square (Sohankar *et al.* [17], for $B = 0.05$) implying separation angle, $\theta_s = 135^\circ$, measured from the forward stagnation point. Regarding the location of separation points at the onset of separation from a square having sharp corners, a fundamental question naturally comes to the mind. What is the value of separation angle for $Re = Re_s$; is it 135 or 180° ? The earlier studies appear to have overlooked this important aspect of initial separation. In the present numerical investigation, these issues are addressed through careful finite-element computations performed with very fine non-uniform mesh. Also compared are the steady flow characteristics of square and elliptic cylinders of various aspect ratios whose major axes are oriented normal to the free-stream. The aspect ratio, AR , of an elliptic cylinder is the ratio of the lengths of the minor and major axes. A stabilized Petrov–Galerkin finite-element formulation accommodating equal-order bilinear interpolation for velocity and pressure is used. The study is conducted for a low blockage of 0.01 .

The outline of the remainder of the article is as follows. In Section 2, the governing equations for incompressible fluid flow are reviewed. The finite-element formulation involving SUPG and PSPG stabilizations is presented in Section 3. The definition of the problem and finite-element mesh are described in Sections 4 and 5, respectively. Validation of the present computations and convergence study for the mesh are presented in Section 6. The main results are presented and discussed in Section 7. The separation Reynolds number is determined for the unbounded flow. The most important contribution of the present investigation is the observation that the separation angle at Re_s equals 180° . Also, the effects of Re on the characteristic flow quantities are studied. Empirical relations are proposed for the bubble length, width and drag force. Finally, the flow characteristics of square cylinder are compared with those of circular and elliptic cylinders having the same characteristic dimension. In Section 8, a few concluding remarks are made.

2. THE GOVERNING EQUATIONS

Let $\Omega \subset \mathbb{R}^{n_{sd}}$ be the spatial domain, where $n_{sd} = 2$ is the number of space dimensions. The boundary of Ω is denoted by Γ and is assumed to be piecewise smooth. The closure of the domain is denoted by $\bar{\Omega}$. The spatial coordinates are denoted by $\mathbf{x} (=x, y)$. The equations governing the steady flow of an incompressible fluid of density, ρ , are:

$$\rho(\mathbf{u} \cdot \nabla \mathbf{u} - \mathbf{f}) - \nabla \cdot \boldsymbol{\sigma} = 0 \quad \text{on } \Omega, \quad (1)$$

$$\nabla \cdot \mathbf{u} = 0 \quad \text{on } \Omega. \quad (2)$$

Here $\mathbf{u} (=u, v)$, \mathbf{f} and $\boldsymbol{\sigma}$ denote the fluid velocity, body force per unit volume and the Cauchy stress tensor, respectively. The stress is the sum of its isotropic and deviatoric parts:

$$\boldsymbol{\sigma} = -p\mathbf{I} + \mathbf{T}, \quad \mathbf{T} = 2\mu\boldsymbol{\varepsilon}(\mathbf{u}), \quad \boldsymbol{\varepsilon}(\mathbf{u}) = \frac{1}{2}((\nabla \mathbf{u}) + (\nabla \mathbf{u})^T), \quad (3)$$

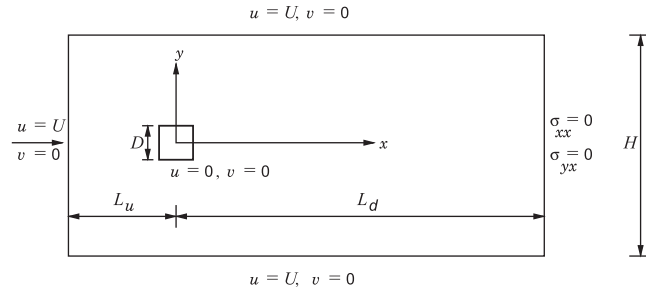


Figure 1. Problem definition for the steady flow past a stationary square cylinder at zero incidence.

where p , \mathbf{I} , μ and $\boldsymbol{\varepsilon}$ are the pressure, identity tensor, dynamic viscosity of the fluid and strain rate tensor, respectively. Both the Dirichlet- and Neumann-type boundary conditions are accounted for and are represented as

$$\mathbf{u} = \mathbf{g} \text{ on } \Gamma_g, \quad \mathbf{n} \cdot \boldsymbol{\sigma} = \mathbf{h} \text{ on } \Gamma_h, \quad (4)$$

respectively, where Γ_g and Γ_h are complementary subsets of the boundary Γ , \mathbf{n} is its unit normal vector and \mathbf{h} is the surface traction vector. In the present simulations, we have employed the towing tank boundary condition (see Figure 1) on the lateral walls of the domain. This boundary condition involves prescribed free-stream speed condition on the upstream as well as lateral boundaries. No-slip boundary condition is applied on the surface of the cylinder. At the downstream boundary, a Neumann condition for velocity is specified that corresponds to the stress-free condition.

3. THE FINITE-ELEMENT FORMULATION

The spatial domain Ω is discretized into non-overlapping subdomains Ω^e , $e = 1, 2, \dots, n_{\text{el}}$, where n_{el} is the number of elements. Let $\mathcal{S}_{\mathbf{u}}^h$ and \mathcal{S}_p^h be the finite-dimensional trial function spaces for velocity and pressure, respectively, and the corresponding weighting function spaces are denoted by $\mathcal{V}_{\mathbf{u}}^h$ and \mathcal{V}_p^h . The stabilized finite-element formulation of the conservation equations (1) and (2) is written as follows: find $\mathbf{u}^h \in \mathcal{S}_{\mathbf{u}}^h$ and $p^h \in \mathcal{S}_p^h$ such that $\forall \mathbf{w}^h \in \mathcal{V}_{\mathbf{u}}^h$, $q^h \in \mathcal{V}_p^h$

$$\begin{aligned} & \int_{\Omega} \mathbf{w}^h \cdot \rho(\mathbf{u}^h \cdot \nabla \mathbf{u}^h - \mathbf{f}) d\Omega + \int_{\Omega} \boldsymbol{\varepsilon}(\mathbf{w}^h) : \boldsymbol{\sigma}(p^h, \mathbf{u}^h) d\Omega + \int_{\Omega} q^h \nabla \cdot \mathbf{u}^h d\Omega \\ & + \sum_{e=1}^{n_{\text{el}}} \int_{\Omega^e} \frac{1}{\rho} (\tau_{\text{SUPG}} \rho \mathbf{u}^h \cdot \nabla \mathbf{w}^h + \tau_{\text{PSPG}} \nabla q^h) \cdot [\rho(\mathbf{u}^h \cdot \nabla \mathbf{u}^h - \mathbf{f}) - \nabla \cdot \boldsymbol{\sigma}(p^h, \mathbf{u}^h)] d\Omega^e \\ & + \sum_{e=1}^{n_{\text{el}}} \int_{\Omega^e} \delta \nabla \cdot \mathbf{w}^h \rho \nabla \cdot \mathbf{u}^h d\Omega^e = \int_{\Gamma_h} \mathbf{w}^h \cdot \mathbf{h}^h d\Gamma. \end{aligned} \quad (5)$$

In the variational formulation given by Equation (5), the first three terms and the right-hand side constitute the Galerkin formulation of the problem. The first series of element level integrals are the SUPG and PSPG stabilization terms added to the variational formulations of the momentum and the continuity equations, respectively. The second series of element-level integrals is added for numerical stability at high Reynolds numbers. This is a least-squares term based on the continuity equation. More details on the finite-element formulation can be found in Tezduyar *et al.* [18].

4. PROBLEM SET-UP

The square cylinder, with edge length of D , is placed in a computational domain whose outside boundary is a rectangle (see Figure 1). The origin of the Cartesian coordinate system coincides

with the center of the cylinder. The flow is from left to right and positive x axis is in the downstream direction. The boundary conditions associated with the present simulations and described in Section 2 are also shown in the figure. The sidewalls are equidistant from the origin of the coordinate system; the distance between the sidewalls, H , being $100D$ gives a blockage of 0.01. The distances of the upstream and downstream boundaries from the origin of the coordinate system are denoted by L_u and L_d , respectively. For the present study, $L_u = 80D$ and $L_d = 100D$ are sufficiently large to produce solutions free from the effects of the inlet and exit boundary conditions. The Reynolds number, $Re (=UD/\nu)$, is based on the edge length and free-stream speed.

5. THE FINITE-ELEMENT MESH

The non-uniform, multi-block finite-element mesh consisting of the bilinear quadrilateral elements is shown in Figure 2. The number of nodes and elements are 158 138 and 157 108, respectively. The mesh has been constructed by combining five blocks; a central square block containing the cylinder and four neighboring rectangular blocks located to the left, right, top and bottom of the central block. Each of these neighboring blocks consists of a Cartesian non-uniform structured mesh with uniform (constant) but different increments in element sizes along the coordinate directions. The top and bottom blocks are mirror images of each other. The edge length of the central block is $4D$ and it consists of 65 736 nodes and 65 072 elements. Within the central block, the spacing between circumferential grid lines follows non-uniform increment away from the cylinder. The radial grid lines in the central block maintain uniform spacing except in the immediate neighborhood of the sharp corners. To reduce the effects of corner singularity, the node next to the sharp corners on either side is located at a small x or y distance of $0.001D$ from the corners. The number of nodes, N_t , on the cylinder surface or any other circumferential grid line equals 664. A radial thickness h_1^r of $0.0005D$ is employed for the first layer of elements located on the cylinder surface.

6. VALIDATION OF METHOD AND CONVERGENCE OF RESULTS

6.1. Comparison with the earlier studies

The comparison of the results from the present study, for $Re=5$ and 40, with earlier results is shown in Table I. The current predictions are in excellent agreement (within 2.5%) with those reported by Dhiman *et al.* [16] for $B=0.05$. The present results are in close agreement (within 3%)

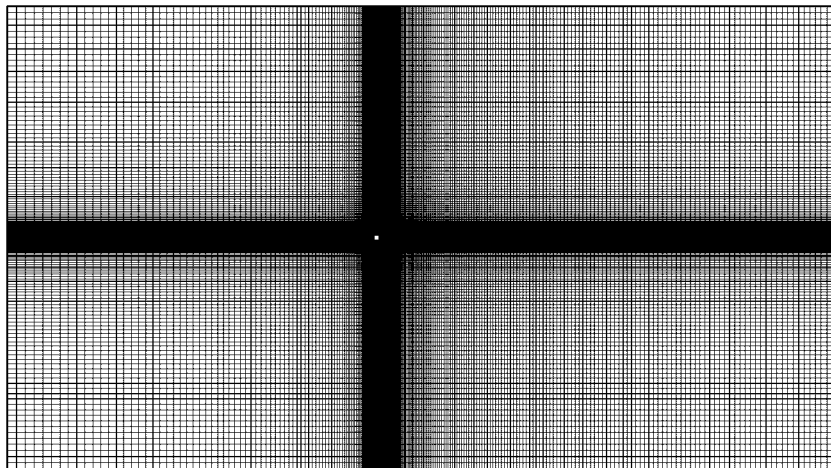


Figure 2. $B=0.01$ steady flow past a stationary square cylinder at zero incidence: the finite-element mesh consisting of 158 138 nodes and 157 108 bilinear quadrilateral elements.

Table I. Steady flow past a stationary square cylinder at zero incidence: comparison of predicted flow parameters with the earlier numerical efforts at $Re=5$ and 40.

Studies	B	L/D		C_d	
		$Re=5$	40	5	40
Paliwal <i>et al.</i> [14]	0.067	0.3000	2.7000	4.8140	1.8990
Present	0.067	0.3163	2.7348	5.2641	1.8565
Dhiman <i>et al.</i> [16]	0.050	0.3090	2.8220	4.8400	1.7670
Present	0.050	0.3166	2.8065	4.9535	1.7871

Table II. Steady flow past a stationary square cylinder at zero incidence ($L_u=80D$, $L_d=100D$ and $B=0.01$): details of the various meshes used for the mesh convergence study as well as the flow parameters obtained at $Re=10$ and 40.

Mesh	Nodes	Elements	N_t	L/D		C_d	
				$Re=10$	40	10	40
M1	79 070	78 360	432	0.6395	2.8968	3.0772	1.6764
M2	158 138	157 108	664	0.6295	2.8638	3.0700	1.6697
M3	313 942	312 512	784	0.6267	2.8552	3.0683	1.6680

For each mesh, $h_1^r = 0.0005D$.

with those of Paliwal *et al.* [14] for $Re=40$. However, there are discrepancies between the two sets of results for $Re=5$.

6.2. Mesh convergence

To establish the adequacy of the mesh, computations were performed for the flow at $Re=10$ and 40 on several meshes with different spatial resolutions. The extent of spatial domain is kept same in all the cases ($L_u=80D$, $L_d=100D$ and $B=0.01$). Table II lists the details of the three meshes M1, M2 and M3 utilized for the convergence study. The spatial resolution increases from mesh M1 to M3. Starting from mesh M1, each successive mesh is generated by incorporating uniform global refinement such that the total number of nodes and elements increases by a factor of 2, approximately. Table II also summarizes the results of mesh convergence study. It is observed that refining the mesh beyond M2 does not have any appreciable influence on the flow characteristics. Mesh M2 is, therefore, used for all computations in the present work.

7. RESULTS

The steady flow characteristics of a symmetric square cylinder is studied for various Re ($Re \leq 40$). To simulate unbounded flow, the blockage is kept very low ($B=0.01$). Comparison is presented for results for elliptic cylinders of aspect ratios 0.2, 0.5, 0.8 and 1 with major axis normal to the incoming flow. All computations are carried out with 4-noded, bilinear, equal-in-order interpolation functions for velocity and pressure. A 2×2 points Gauss–Legendre quadrature formula is employed for numerical integration. The linearized algebraic equation system resulting from the finite-element discretization of the fluid flow equations are solved by a matrix-free implementation of the Generalized Minimal RESidual method (GMRES) [19]. To accelerate the convergence rate of GMRES, a diagonal preconditioner has been used.

7.1. Steady flow past a square cylinder with sharp corners

7.1.1. Development of the wake with Re . Figure 3 illustrates the development of separation bubble with Re . Similar to the circular [12] and symmetric elliptic cylinders [20], the separation bubble

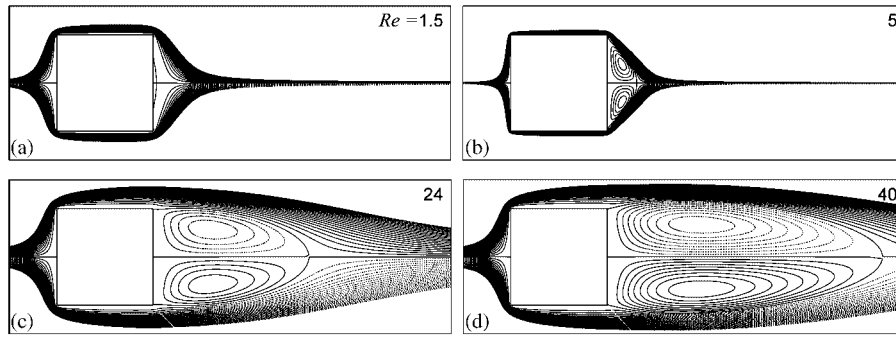


Figure 3. Steady flow past a symmetric square cylinder for $B=0.01$: streamline contours showing the development of separation bubble with Re .

of a square cylinder comprises of two symmetric and counter-rotating recirculation zones. The region of recirculation is bounded by closed streamlines and is attached to the rear surface of the cylinder. The streamwise and transverse enlargement of the bubble with Re is evident from the figure. From the figure it is observed that for $Re \geq 5$, the flow separates at the sharp edges. However, for $Re = 1.5$, the flow seems to be attached at the corners. In the next subsection, we attempt to determine the critical Re for the onset of flow separation.

7.1.2. θ_s at the onset of separation and θ_s-Re relationship. The extremely small dimension of the separation bubble at inception poses difficulty in accurate determination of the location of separation points. Lighthill [21] pointed out that a steady separated flow is characterized by the presence of an even number of points with zero vorticity ($\omega=0$) and located on the body surface. These are alternate points of reattachment and separation. In case of a symmetric square cylinder, the attached flow is characterized by the presence of two such points: forward and rear stagnation. The appearance of two more zero-vorticity points on the cylinder implies separated flow. Figure 4(a) shows the surface vorticity distribution for $Re=1.15-1.2$. Figure 4(b) shows the close-up of the vorticity distribution for regions close to the base point. The circumferential angle, θ , as well as separation angle, θ_s , are measured counterclockwise from the forward stagnation point. The zero-vorticity points other than at cylinder base (see Figure 4(b)) represent the lower ($\theta < 180^\circ$) and upper ($\theta > 180^\circ$) separation points. The $\omega-\theta$ profile for $Re \leq 1.16$ crosses the zero-vorticity line only at the base point ($\theta = 180^\circ$) implying attached flow. The presence of zero-vorticity points above and below the base point at $Re \geq 1.17$ indicates separated flow. This shows that Re_s lies between 1.16 and 1.17. An obvious conclusion drawn from Figure 4(b) is that the flow separation initiates from the base point, and not from the rear corners. The distribution of vorticity along the cylinder surface, shown in Figure 4(a), reveals antisymmetry about the base point. The maximum and minimum values of vorticity are attained at the lower and upper leading tips, respectively. Subsequently, ω drops (or rises) to much smaller (or larger) values. Along most of the lower and upper surfaces, the vorticity is almost constant. The fact that the flow is attached to the upper and lower surfaces is also apparent from the observation that there is no sign change of ω along the lateral surfaces.

To determine the separation Re from the surface vorticity distribution, the vorticity gradient, $\partial\omega/\partial\theta$, is evaluated at the base point. Its variation with Re is shown in Figure 5. The $\partial\omega/\partial\theta-Re$ curve is linear and the vorticity gradient vanishes at $Re = Re_s$. Using linear interpolation, we obtain $Re_s = 1.16$.

The vorticity distribution curves shown in Figure 4 are utilized to determine the separation angle for various Reynolds numbers. Figure 6 shows the variation of separation angle of the flow with Re . The θ_s-Re curve is characterized by a sharp fall in the separation angle near the onset Re . For $Re > 5$, $\theta_s \approx 135^\circ$, i.e. the separation points are fixed to the rear corners of the square cylinder.

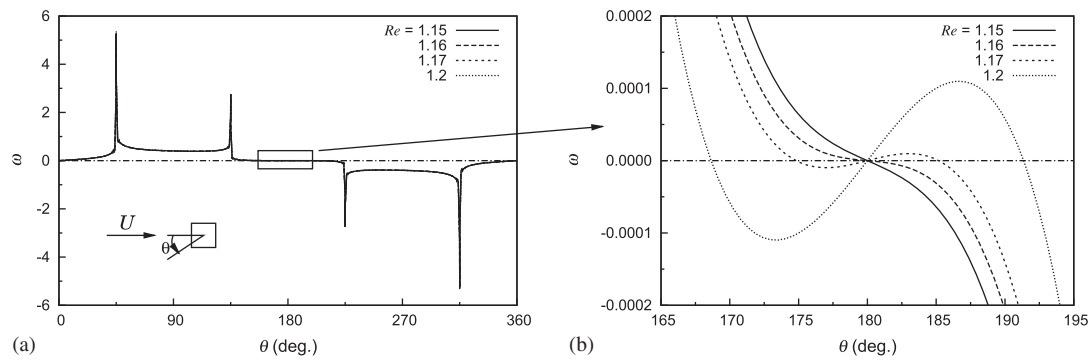


Figure 4. Steady flow past a symmetric square cylinder for $B=0.01$: (a) the surface vorticity distribution for $Re=1.15-1.2$ and (b) close-up of the highlighted region in (a). The circumferential angle θ is measured counterclockwise from the forward stagnation point. The base point corresponds to $\theta=180^\circ$.

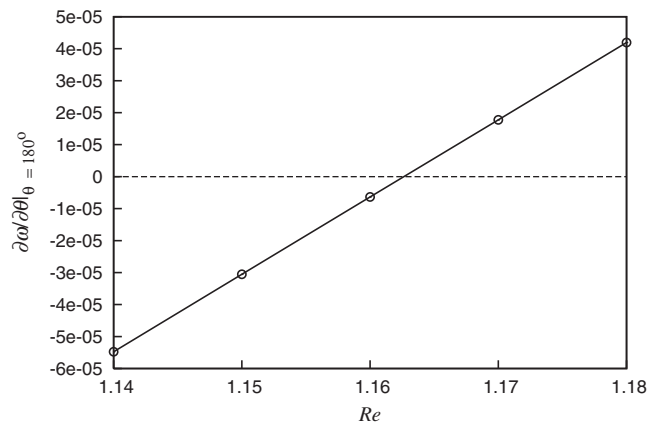


Figure 5. Steady flow past a symmetric square cylinder at $Re=1.14-1.18$ for $B=0.01$: Reynolds number variation of $\partial\omega/\partial\theta$ computed at the base point.

7.1.3. $L-Re$ relationship and the separation Reynolds number. The u velocity distribution along the wake centerline, for various Re , is shown in Figure 7(a). The zero-velocity points in the $u-Re$ curves represent the base and wake stagnation points lying on the wake centerline. L is the streamwise distance between them and represents the length of the recirculation bubble. Presence of a zone of recirculation at $Re=1.25$ is evident from Figure 7(a). Figure 7(b) shows the variation of bubble length with Re . It is observed that the bubble length increases approximately linearly with Re . The linear $L/D-Re$ relationship was also observed by Breuer *et al.* [10] and Sharma and Eswaran [15], for $B=0.125$ and 0.05 , respectively. The relationship between L/D and Re for the unbounded flow is expressed by the following empirical equation obtained via least-squares curve fit

$$L/D = -0.0783 + 0.0724Re \quad \text{for } Re_s \leq Re \leq 40. \quad (6)$$

By extrapolation of the bubble length to zero, we find that $Re_s = 1.15$. This value is very close to the one ($= 1.16$) obtained from the surface vorticity distribution. While Breuer *et al.* [10] found no separation of flow for $Re \leq 1$ using $B=0.125$, the streamline plots presented by Sharma and Eswaran [15] imply that $1 < Re_s < 2$ for $B=0.05$.

7.1.4. Variation of the bubble width with Re . Figure 8 illustrates the variation of bubble width with Re for $Re=1.17-40$. It is found that up to $Re \approx 23$, the bubble width corresponds to the vertical distance between the upper and lower separation points. w increases sharply with Re near the

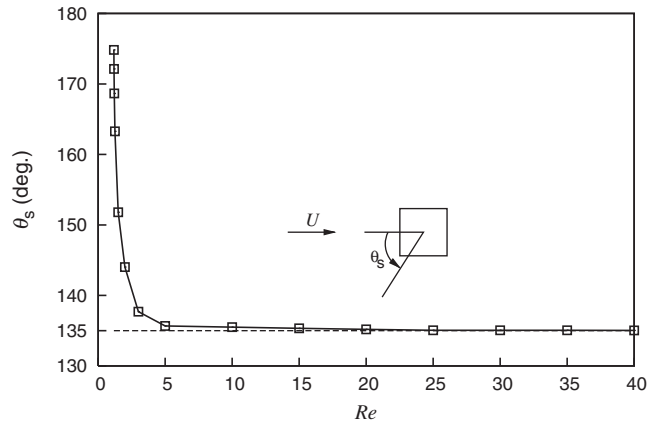


Figure 6. Steady flow past a symmetric square cylinder for $B=0.01$: the variation of separation angle with Re . A Reynolds number range of 1.17–40 is used. The separation angle is measured counterclockwise from the forward stagnation point.

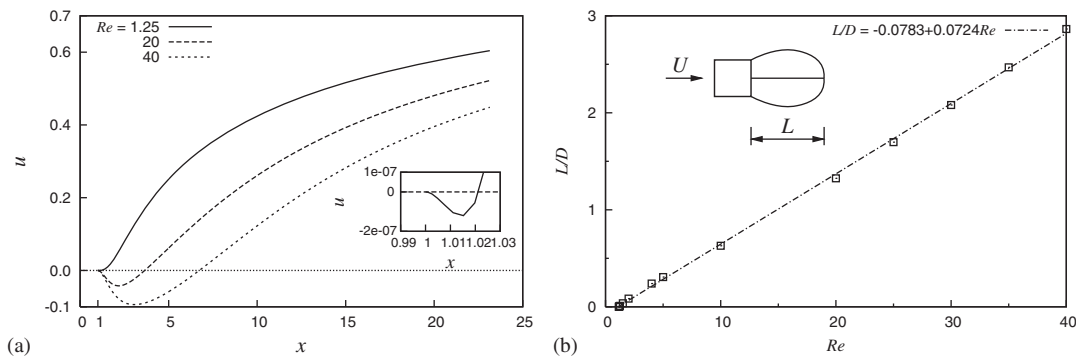


Figure 7. Steady flow past a symmetric square cylinder for $B=0.01$: (a) u velocity distribution along the wake centerline for various Re and (b) variation of the bubble length with Re . The inset in (a) shows the u velocity distribution in close-up for $Re=1.25$.

onset of separation. It is, approximately, equal to the edge length of the cylinder for $Re \approx 5$ to 23. The widening of the bubble beyond D is found to initiate between $Re=23$ and 24. Subsequently, w increases approximately linearly with increasing Re . The best fit curve for the linear part of the $w/D-Re$ profile is expressed by the following empirical equation:

$$w/D = 0.7677 + 0.0101 Re. \quad (7)$$

The above equation is valid for $24 \leq Re \leq 40$.

7.1.5. Variation of the drag coefficient with Re . The drag coefficient of a bluff body decreases with increasing Re . The decrease in C_d is attributed to the increasing pressure recovery at the cylinder base. The drag coefficient of a square decreases with Re (Figure 9(a)) according to the following empirical relationship:

$$C_d = 0.7496 + 10.5767 Re^{-0.66} \quad \text{for } 2 \leq Re \leq 40. \quad (8)$$

The above equation is obtained via a least-squares curve fit. The decay with Re of both C_{dp} and C_{dv} is illustrated in Figure 9(b). The curves for pressure and viscous drag are nearly parallel. The figure also reveals the relative dominance of the pressure drag over its viscous counterpart.

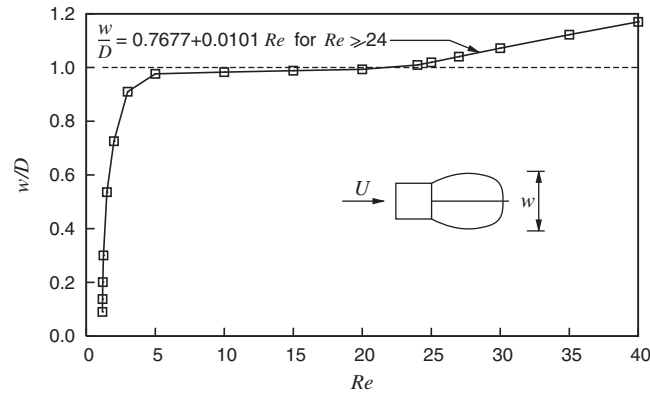


Figure 8. Steady flow past a symmetric square cylinder for $B=0.01$: variation of the bubble width with Re . The width is measured between the separation streamlines in a direction normal to the flow.

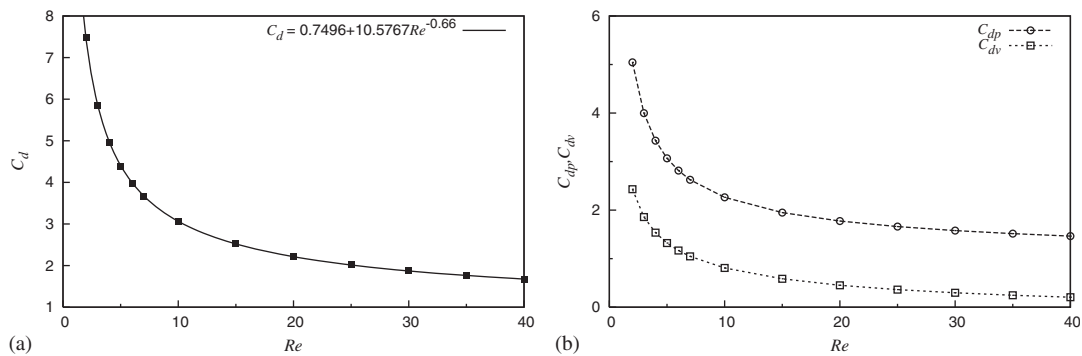


Figure 9. Steady flow past a symmetric square cylinder for $B=0.01$: variation of the (a) total drag coefficient and (b) pressure and viscous drag components with Re for $2 \leq Re \leq 40$.

7.2. Unsteady flow past a symmetric square cylinder

Results are presented for unsteady flow past a stationary square cylinder at zero incidence for $B=0.05$ and $60 \leq Re \leq 150$. For the unsteady flow computations, the time step used is 0.03. Time is non-dimensionalized using the free-stream speed and edge length of the cylinder. The Crank–Nicholson scheme is employed for time stepping.

7.2.1. Comparison of the integral parameters with earlier results. For $B=0.05$, comparison of the predicted integral parameters with earlier numerical results available in the literature for a stationary square cylinder at $Re=100$ is presented in Table III. The results reported by Darekar and Sherwin [22] from three-dimensional computations, for $B=0.023$, are also shown. The predicted time-averaged ($\overline{C_d}$) and root mean square or r.m.s. ($C_{d,rms}$) drag coefficients as well as Strouhal number, St , compare favorably with the existing results. All the aerodynamic coefficients, including St , are non-dimensionalized using D and free-stream speed. The St value from Robichaux *et al.* [7] is slightly higher than those reported by others. A scatter in the values of r.m.s. lift coefficient, $C_{l,rms}$, is evident from the table. The predictions by Sohankar *et al.* [6] and Singh *et al.* [23] are on the lower side, whereas those by Darekar and Sherwin [22], Sharma and Eswaran [15] and Sahu *et al.* [24] are on the higher side. The value from the present effort is in excellent agreement with the one reported by Sharma and Eswaran [15]. The difference between the two values is less than 0.3%.

Table III. Unsteady two-dimensional flow past a stationary square cylinder at zero incidence: comparison of various integral parameters at $Re=100$.

Studies	B	$\overline{C_d}$	$C_{d_{rms}}$	$C_{l_{rms}}$	St
Sohankar <i>et al.</i> [6]	0.050	1.4770		0.1560	0.1460
Robichaux <i>et al.</i> [7]	0.056	1.5300			0.1540
Darekar and Sherwin [22] (3D)	0.023	1.4860		0.1860	0.1460
Sharma and Eswaran [15]	0.050	1.4936	0.0054	0.1922	0.1488
Singh <i>et al.</i> [23]	0.050	1.5100		0.1600	0.1470
Sahu <i>et al.</i> [24]	0.050	1.4878		0.1880	0.1486
Present	0.050	1.5287	0.0055	0.1928	0.1452

The results reported by Darekar and Sherwin [22] were obtained from three-dimensional (3D) simulations.

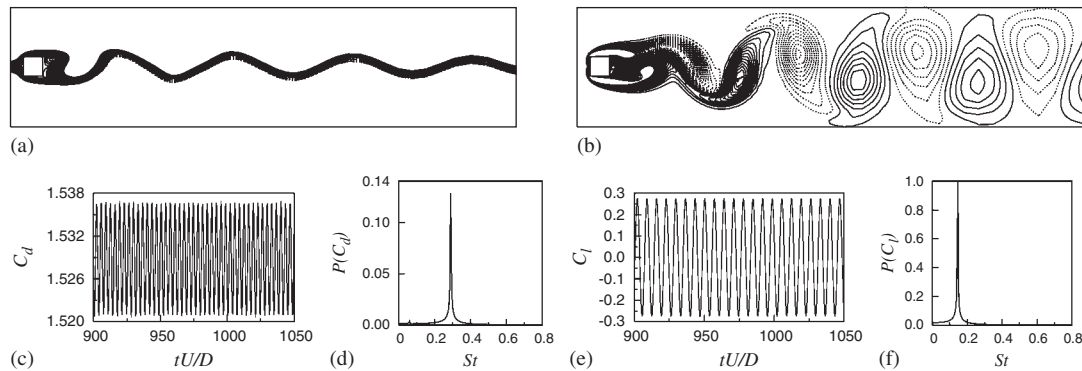


Figure 10. $Re=100$ unsteady flow past a symmetric square cylinder for $B=0.05$: the (a) instantaneous streamlines; (b) instantaneous vorticity field; (c) time series of C_d ; (d) power spectrum of C_d signal; (e) time series of C_l ; and (f) power spectrum of C_l signal.

7.2.2. The unsteady flow at $Re=100$. In this section, results are presented for unsteady flow at $Re=100$ past a stationary square cylinder at zero incidence. The instantaneous streamlines are shown in Figure 10(a). Figure 10(b) shows the corresponding instantaneous vorticity field and characterizes the Karman vortex street of the shed vortices. Time histories of the drag and lift coefficients after establishment of the dynamic steady state are presented in Figures 10(c) and (e), respectively. The fluctuating component of lift is significantly larger than its drag counterpart. The power spectra determined from the time histories of drag (Figure 10(d)) and lift (Figure 10(f)) display single dominant peak for each case. The lift force oscillates at the shedding frequency, whereas the drag force varies with twice the shedding frequency.

7.2.3. Variation of the integral parameters with Re . The variation of non-dimensional vortex-shedding frequency, St , and primary wavelength, λ , of a square cylinder with Re is shown in Figure 11 for $60 \leq Re \leq 150$. Consistent with the earlier observations by Robichaux *et al.* [7] and Sharma and Eswaran [15], a monotonic rise in the shedding frequency with Re is observed. The inter-vortex spacing between the shed vortices along each row of the vortex street is estimated from the relationship $\lambda/D = 1/St$ as proposed by Vorobieff *et al.* [25]. A decrease in λ with increasing Re is observed from Figure 11. Using least-squares curve fit, the following empirical equation is proposed for the prediction of St for a square cylinder

$$St = 0.1774 - 3.2242/Re \quad \text{for } 60 \leq Re \leq 130. \quad (9)$$

The variation of aerodynamic coefficients with Re is shown in Figure 12. Figure 12(a) indicates that $\overline{C_d}$ initially decreases and then increases with increasing Re , whereas $C_{d_{rms}}$ increases monotonically (see also Sharma and Eswaran [15]). In contrast, both $C_{l_{max}}$ (amplitude of lift) and $C_{l_{rms}}$ exhibit monotonic increase with Re (Figure 12(b)). The increase in $C_{l_{max}}$ and $C_{l_{rms}}$ with

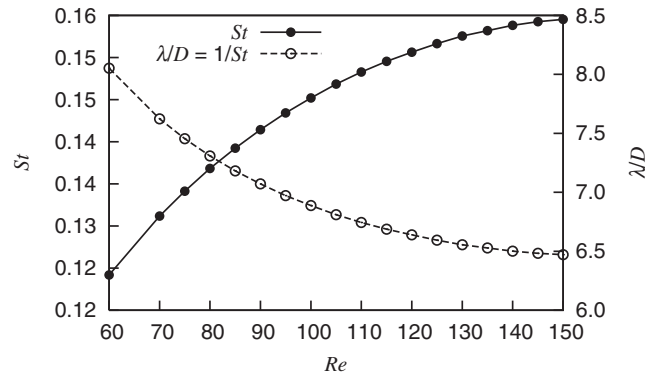


Figure 11. Unsteady flow past a symmetric square cylinder for $B=0.05$: variation of the Strouhal number and primary wavelength, λ , with Re for $60 \leq Re \leq 150$.

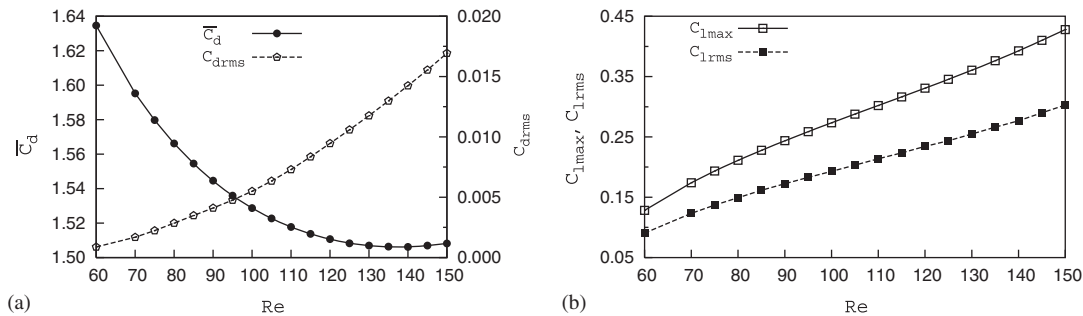


Figure 12. Unsteady flow past a symmetric square cylinder for $B=0.05$: variation of (a) $\overline{C_d}$, $C_{d_{rms}}$ and (b) $C_{l_{max}}$, $C_{l_{rms}}$ with Re for $60 \leq Re \leq 150$.

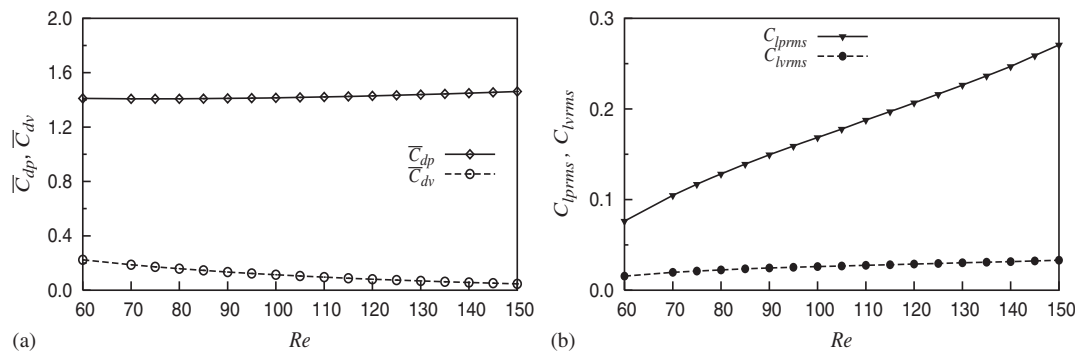


Figure 13. Unsteady flow past a symmetric square cylinder for $B=0.05$: variation of (a) $\overline{C_{dp}}$, $\overline{C_{dv}}$ and (b) $C_{l_{prms}}$, $C_{l_{vrms}}$ with Re for $60 \leq Re \leq 150$.

Re is approximately linear. For the range of Re considered, the time-averaged pressure drag, $\overline{C_{dp}}$, is virtually constant (Figure 13(a)). $\overline{C_{dp}}$ is an order of magnitude larger than the time-averaged viscous drag, $\overline{C_{dv}}$. As can be seen from Figure 13(b), the r.m.s. of viscous lift, $C_{l_{vrms}}$, remains fairly constant with increasing Re , whereas r.m.s. of pressure lift, $C_{l_{prms}}$, exhibits approximate linear increase.

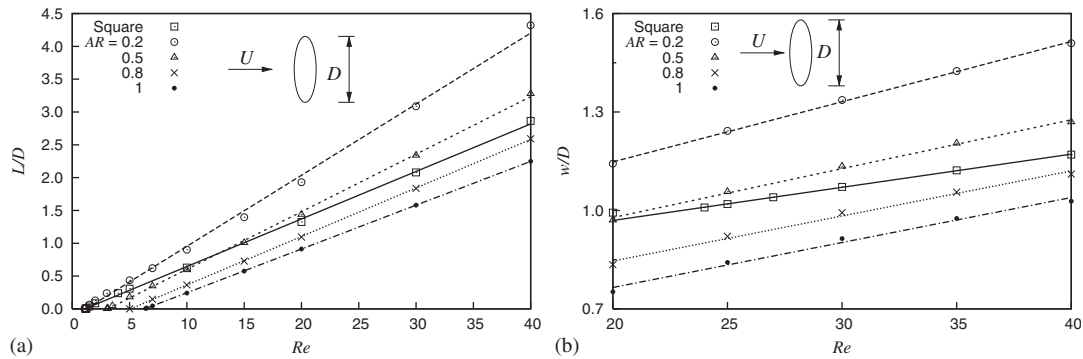


Figure 14. Steady flow past symmetric square and elliptic cylinders of $AR=0.2-1$ for $B=0.01$: variation of the bubble (a) length and (b) width with Re . The major axes of elliptic cylinders are perpendicular to the free-stream.

7.3. Effect of sharp corners

Recently Sen *et al.* [12, 20] studied, for low blockage, the steady flow past circular (aspect ratio, $AR=1$) as well as symmetric and asymmetric elliptic cylinders of aspect ratios 0.2, 0.5 and 0.8. The Re is based on the length along the major axis, D , which also represents the diameter of circular cylinder. All results presented in this section for elliptic cylinders correspond to the cylinder configuration of 90° incidence, i.e. the major axis of the elliptic cylinder is perpendicular to the free-stream. The results for bubble length as well as width of elliptic cylinders in the unbounded medium are presented in Figure 14. For elliptic cylinders, Figures 15 and 16 show the separation angle and drag coefficient, respectively. They are compared with the results for a square cylinder. Interesting observations are made from the comparisons. An essential feature of the symmetric separation is the linear $L/D-Re$ variation. This is irrespective of the bodies having smooth contours or sharp corners (Figure 14(a)). The bubble length of a square cylinder is larger than the one for a circular cylinder. This was shown earlier by Sharma and Eswaran [15] for $B=0.05$. The slope of $L/D-Re$ profiles is maximum ($=0.1083$) for the $AR=0.2$ cylinder and minimum ($=0.0667$) for a circle. For a square, the slope is 0.0724. For $20 \leq Re \leq 40$, Figure 14(b) shows that the maximum and minimum bubble widths are associated with $AR=0.2$ and 1, respectively. The bubble width of a square at a given Re is larger than the value obtained for a circle. It was shown in Section 7.1.2 that the separation angle for a square cylinder decreases with Re near the onset of separation and approaches the fixed location of rear corners for $Re > 5$, approximately. In contrast, the separation angle for smooth cylinders decreases monotonically with Re as evident from Figure 15 (also see Sen *et al.* [12, 20]).

Figure 16(a) demonstrates that the bluff body with corners results in higher drag than a bluff body with smooth contours of identical characteristic dimension. For square and elliptic cylinders, Figure 16(b) shows the variation of C_{dp}/C_{dv} with Re for $5 \leq Re \leq 40$. C_{dp}/C_{dv} increases approximately linearly with Re for the circular and elliptic cylinders. For a square cylinder, the variation is, however, non-linear. As is apparent from Figure 16(b), the pressure drag dominates over its viscous counterpart for each geometry. This effect is more pronounced with increasing Re . Interestingly, the observation that drag of a square cylinder is maximum among all the cross-sections does not hold for the ratio C_{dp}/C_{dv} . When Re is fixed, C_{dp}/C_{dv} is maximum for $AR=0.2$ and minimum for $AR=1$ (circle); for a square, the ratio lies in between the ones for $AR=0.2$ and 1.

Table IV summarizes various flow parameters obtained for the square and elliptic cylinders. Among the various cross-sections of interest, the Reynolds number for the onset of flow separation is largest for circular cylinder ($Re_s=6.29$). The smallest $Re_s(=1.05)$ is associated with the elliptic cylinder of $AR=0.2$. The larger bubble dimensions and drag along with a much smaller separation Re renders a square cylinder more bluff than an equivalent circular cylinder of same characteristic dimension.

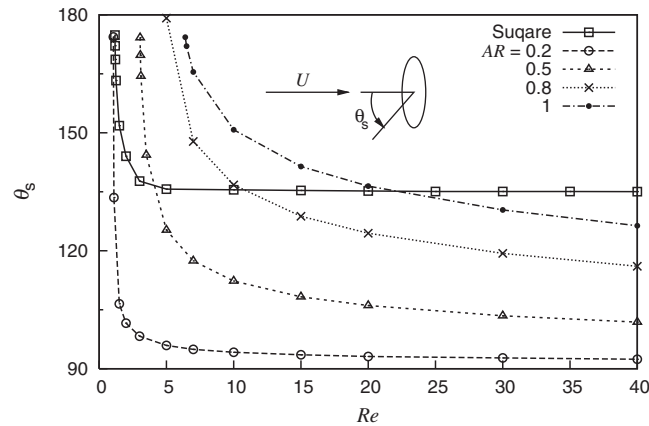


Figure 15. Steady flow past symmetric square and elliptic cylinders of $AR=0.2-1$ for $B=0.01$: variation of the separation angle with Re . The major axes of elliptic cylinders are perpendicular to the free-stream.

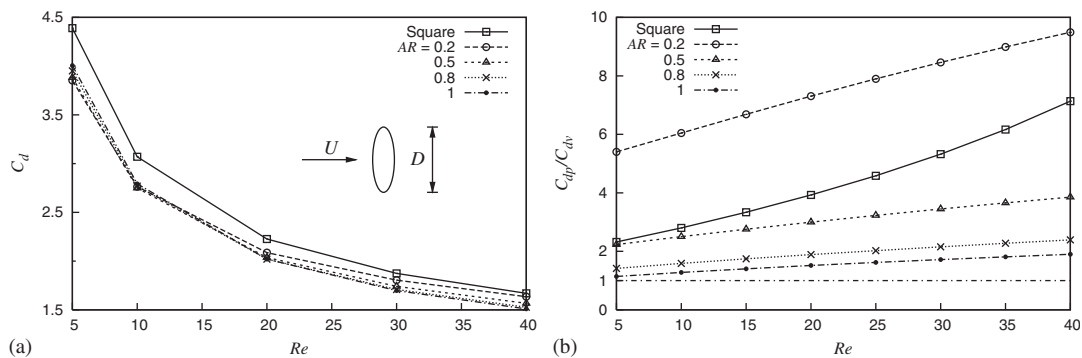


Figure 16. Steady flow past symmetric square and elliptic cylinders of $AR=0.2-1$ for $Re=5-40$ and $B=0.01$: variation of (a) C_d and (b) C_{dp}/C_{dv} ratio with Re . The major axes of elliptic cylinders are perpendicular to the free-stream.

Table IV. Steady flow past symmetric square and elliptic cylinders of $AR=0.2-1$ for $B=0.01$: comparison of predicted flow parameters. The major axes of elliptic cylinders are perpendicular to the free-stream.

	Square		AR=0.2		AR=0.5		AR=0.8		AR=1	
Re_s	1.15		1.05		3.02		4.99		6.29	
	$Re=5$	40	5	40	5	40	5	40	5	40
L/D	0.3075	2.8638	0.4349	4.3201	0.1805	3.2777	0.00075	2.5910		2.2480
w/D		1.1636		1.5097		1.2694		1.1108		1.0280
C_d	4.3896	1.6697	3.8532	1.6351	3.8830	1.5671	3.9510	1.5265	4.005	1.5099

8. CONCLUSIONS

A stabilized finite-element formulation is used to predict the steady flow past a symmetric square cylinder for a low blockage of 0.01 and Reynolds numbers up to 40. The wake is closed, symmetric about the x axis and remains attached to the rear surface of the cylinder in the regime of steady separated flow. The separation bubble elongates approximately linearly with Re . By using the linearity of bubble length with Re , it is found that $Re_s=1.15$ for the unbounded flow. This Re_s value is in close agreement with the one predicted ($=1.16$) using the surface vorticity distribution.

Separation angle, θ_s , (measured from the forward stagnation point) for various Re are determined from the surface vorticity distribution. Sen *et al.* [12, 20] recently demonstrated for the circular and symmetric elliptic cylinders that $\theta_s = 180^\circ$ at the separation Re . The same is found for a square cylinder with sharp corners. The symmetric separation therefore initiates essentially from the base point, irrespective of the sharp or smooth contours of the bluff body. For $Re > 5$, approximately, θ_s approaches its steady flow limit of 135° and the separation points remain fixed to the cylinder rear corners. In contrast, the separation angle for circular and symmetric elliptic cylinders decreases monotonically with Re [12, 20]. The Reynolds number variation of bubble width, w , of a square cylinder shows three distinct phases. In the first part, w increases sharply till Re about 5. The second part stretches to $Re \approx 23$, where w is approximately of the order of the edge length. The final part is characterized by a linear increase of w with Re .

Empirical equations are proposed for the bubble parameters and drag coefficient. The bubble length follows the relationship $L/D = -0.0783 + 0.0724 Re$ for $Re_s \leq Re \leq 40$. For $Re \geq 24$, the bubble widens as $w/D = 0.7677 + 0.0101 Re$. The dependence of the drag coefficient on Reynolds number is expressed as $C_d = 0.7496 + 10.5767 Re^{-0.66}$. Flow characteristics of the square cylinder are compared with those of elliptic cylinders of aspect ratios 0.2, 0.5, 0.8 and 1 (circle) having the same characteristic dimension as the square. The major axes of elliptic cylinders are normal to the free-stream. Among all the cylinder shapes, the Re_s is smallest ($= 1.05$) for $AR = 0.2$ and largest ($= 6.29$) for a circle. Compared with the circular cylinder, a square gives more drag and larger bubble length as well as width at the same Re . Also, flow separates at a much lower Re from the square cylinder. In general in the steady flow regime, a square cylinder experiences more drag than the circular and elliptic cylinders. For the square cylinder at zero incidence, results are also presented for the unsteady flow for $B = 0.05$ and $60 \leq Re \leq 150$. With increasing Re , the non-dimensional vortex-shedding frequency and r.m.s. values of the aerodynamic forces increase monotonically. In contrast, the time-averaged drag coefficient displays a non-monotonic variation. For $60 \leq Re \leq 130$, the Strouhal number of a square cylinder obeys the relationship $St = 0.1774 - 3.2242/Re$.

REFERENCES

1. Okajima A. Strouhal numbers of rectangular cylinders. *Journal of Fluid Mechanics* 1982; **123**:379–398.
2. Davis RW, Moore EF, Purtell LP. A numerical-experimental study of confined flow around rectangular cylinders. *Physics of Fluids* 1984; **27**:46–59.
3. Davis RW, Moore EF. A numerical study of vortex shedding from rectangles. *Journal of Fluid Mechanics* 1982; **116**:475–506.
4. Franke R, Rodi W, Schöning B. Numerical calculation of laminar vortex-shedding flow past cylinders. *Journal of Wind Engineering and Industrial Aerodynamics* 1990; **35**:237–257.
5. Mukhopadhyaya A, Biswas G, Sundararajan T. Numerical investigation of confined wakes behind a square cylinder in a channel. *International Journal for Numerical Methods in Fluids* 1984; **14**:1473–1484.
6. Sohankar A, Norberg C, Davidson L. Low-Reynolds-number flow around a square cylinder at incidence: study of blockage, onset of vortex shedding and outlet boundary condition. *International Journal for Numerical Methods in Fluids* 1998; **26**:39–56.
7. Robichaux J, Balachandar S, Vanka SP. Three-dimensional floquet instability of the wake of square cylinder. *Physics of Fluids* 1999; **11**:560–578.
8. Saha AK, Biswas G, Muralidhar K. Three-dimensional study of flow past a square cylinder at low Reynolds numbers. *International Journal of Heat and Fluid Flow* 2003; **24**:54–66.
9. Sheard GJ, Fitzgerald MJ, Ryan K. Cylinders with square cross-section: wake instabilities with incidence angle variation. *Journal of Fluid Mechanics* 2009; **630**:43–69.
10. Breuer M, Bernsdorf J, Zeiser T, Durst F. Accurate computations of the laminar flow past a square cylinder based on two different methods: lattice-Boltzmann and finite-volume. *International Journal of Heat and Fluid Flow* 2000; **21**:186–196.
11. Taneda S. Experimental investigation of the wakes behind cylinders and plates at low Reynolds numbers. *Journal of Physical Society of Japan* 1956; **11**:302–307.
12. Sen S, Mittal S, Biswas G. Steady separated flow past a circular cylinder at low Reynolds numbers. *Journal of Fluid Mechanics* 2009; **620**:89–119.
13. Gupta AK, Sharma A, Chhabra RP, Eswaran V. Two-dimensional steady flow of a power-law fluid past a square cylinder in a plane channel: momentum and heat-transfer characteristics. *Industrial and Engineering Chemistry Research* 2003; **42**:5674–5686.
14. Paliwal B, Sharma A, Chhabra RP, Eswaran V. Power law fluid flow past a square cylinder: momentum and heat transfer characteristics. *Chemical Engineering Science* 2003; **58**:5315–5329.

15. Sharma A, Eswaran V. Heat and fluid flow across a square cylinder in the two-dimensional laminar flow regime. *Numerical Heat Transfer A* 2004; **45**:247–269.
16. Dhiman AK, Chhabra RP, Sharma A, Eswaran V. Effects of Reynolds and Prandtl numbers on heat transfer across a square cylinder in the steady flow regime. *Numerical Heat Transfer A* 2006; **49**:717–731.
17. Sohankar A, Norberg C, Davidson L. Simulation of three-dimensional flow around a square cylinder at moderate Reynolds numbers. *Physics of Fluids* 1999; **11**:288–306.
18. Tezduyar TE, Mittal S, Ray SE, Shih R. Incompressible flow computations with stabilized bilinear and linear equal-order-interpolation velocity–pressure elements. *Computer Methods in Applied Mechanics and Engineering* 1992; **95**:221–242.
19. Saad Y, Schultz MH. GMRESS: a generalized minimal residual algorithm for solving nonsymmetric linear systems. *SIAM Journal on Scientific and Statistical Computing* 1986; **7**:856–869.
20. Sen S, Mittal S, Biswas G. Finite-element simulation of steady flow past elliptic cylinders. *Proceedings of the Eighth Asian Computational Fluid Dynamics Conference*, Hong Kong, Paper no. ACFD0035-T007-A-001, 2010.
21. Lighthill MJ. Boundary layer theory. In *Laminar Boundary Layers*, Rosenhead L (ed.). Oxford University Press: Oxford, 1963; 46–103.
22. Darekar RM, Sherwin SJ. Flow past a square-section cylinder with a wavy stagnation face. *Journal of Fluid Mechanics* 2001; **426**:263–295.
23. Singh AP, De AK, Carpenter VK, Eswaran V, Muralidhar K. Flow past a transversely oscillating square cylinder in free stream at low Reynolds numbers. *International Journal for Numerical Methods in Fluids* 2009; **61**:658–682.
24. Sahu AK, Chhabra RP, Eswaran V. Two-dimensional unsteady laminar flow of a power law fluid across a square cylinder. *Journal of Non-Newtonian Fluid Mechanics* 2009; **160**:157–167.
25. Vorobieff P, Goergiev D, Ingber MS. Onset of the second wake: dependence on the Reynolds number. *Physics of Fluids* 2002; **14**:L53–L56.